Geophysical Research Letters

RESEARCH LETTER
10.1029/2020GL088994

Key Points:

- Impact force spectra of debris flows are inverted using high-frequency seismic signals
- Inverted force spectra are coherent with in situ measurements at a force plate and contain information about particle sizes
- Evolution of inverted force spectra of debris flows indicates variations in bed topography

Supporting Information:

- Supporting Information S1

Correspondence to:
S. He and F. Walter
hsm@imde.ac.cn; walter@vaw.baug.ethz.ch

Citation:
Zhang, Z., Walter, F., McArdell, B. W., Wenner, M., Chmiel, M., de Haas, T., & He, S. (2021). Insights from the particle impact model into the high-frequency seismic signature of debris flows. *Geophysical Research Letters*, *48*, e2020GL088994. https://doi.org/10.1029/2020GL088994

Received 27 MAY 2020
Accepted 21 NOV 2020

Insights From the Particle Impact Model Into the High-Frequency Seismic Signature of Debris Flows

Zhen Zhang[1,2,3], Fabian Walter[2,4], Brian W. McArdell[4], Michaela Wenner[2,4], Małgorzata Chmiel[2], Tjalling de Haas[5], and Siming He[1,3,6]

[1]Key Laboratory of Mountain Hazards and Surface Process, Institute of Mountain Hazards and Environment, Chinese Academy of Sciences, Chengdu, China, [2]Laboratory of Hydraulics, Hydrology and Glaciology, ETH Zürich, Zürich, Switzerland, [3]University of Chinese Academy of Sciences, Beijing, China, [4]Swiss Federal Institute for Forest, Snow and Landscape Research WSL, Zürich, Switzerland, [5]Department of Physical Geography, Universiteit Utrecht, Utrecht, The Netherlands, [6]Center for Excellence in Tibetan Plateau Earth Sciences, Chinese Academy of Sciences, Beijing, China

Abstract Debris flows induce seismic ground unrest detectable over large distances. However, recent theoretical description of debris-flow seismograms has yet to be implemented in alarm systems. Here, we test the implications of a particle impact model for debris-flow detection and warning using seismic data. We analyze 14 debris flows at Illgraben, Switzerland, using instantaneous weight measurements, a seismic network and video footage. A novel approach to simulate seismic wave propagation estimates both vertical and horizontal particle impact forces on the ground. Scaling between impact forces, weight, and particle sizes suggests that seismic data identify destructive debris flows with large boulders. Impact force spectra change with bed topography and increase during flow propagation of large events, but decrease for smaller events. This can be explained with the known conveyor mechanism concentrating boulders at the flow front. Our results highlight opportunities to use seismic data for debris-flow research and warning.

Plain Language Summary Debris flows are muddy mixtures of water, sand, and boulders, which move down steep mountain creeks in an uncontrolled way. They are a major threat to human life, properties, and infrastructure. Ground vibrations generated by debris flows contain information on the characteristics of debris flows that are difficult to measure with conventional methods. However, these ground vibrations are complex and challenging to understand so that scientists struggle to use them for quantitative studies. Here we treat the interaction between debris flows and the ground as many particles randomly bouncing off the channel bed. We can thus simulate the ground vibrations generated by such particle/ground impacts for 14 debris flows at Illgraben, Switzerland. Our results show that particle/ground impacts correlate with the weight of the debris flow. For small events, ground vibrations decrease along the flow path. In contrast, for large-volume debris flows, vibrations gradually increase. This is related to sediment erosion and deposition showing how ground vibrations characterize debris flows.

1. Introduction

Debris flows are fast moving mixtures of water and sediments in mountainous regions, with dynamic characteristics intermediate between floods and landslides (Iverson, 1997; Iverson & Vallance, 2001). Triggered in remote locations, temporal and spatial occurrence of debris flows is difficult to predict. This makes their monitoring challenging and limits time-dependent measurements of their dynamics.

Recent advances in environmental seismology provide unique constraints of the dynamics and timing of landslides, rockfalls, and debris flows (e.g., Barrière et al., 2015; Dammeier et al., 2016; Ekström & Stark, 2013; Hibert et al., 2011; Moretti et al., 2012), as well as sediment transport in rivers (Burtin et al., 2010; Gimbert et al., 2014; Tsai et al., 2012). Debris flows are sources of seismic and acoustic signals, which can be used to estimate location and propagation of their flow fronts (Hürlimann et al., 2019; Marchetti et al., 2019; Schimmel et al., 2018; Schimmel & Hübl, 2015, 2016; Walter et al., 2017). However, multiphase flow contributes to complex seismogenesis (e.g., Iverson, 2003) and typical high-frequency seismic signals generated by debris flows are sensitive to small-scale variations in ground structure (e.g., Allstadt, 2013; Hibert et al., 2017; Kean et al., 2015; Ogiso & Yomogida, 2015).

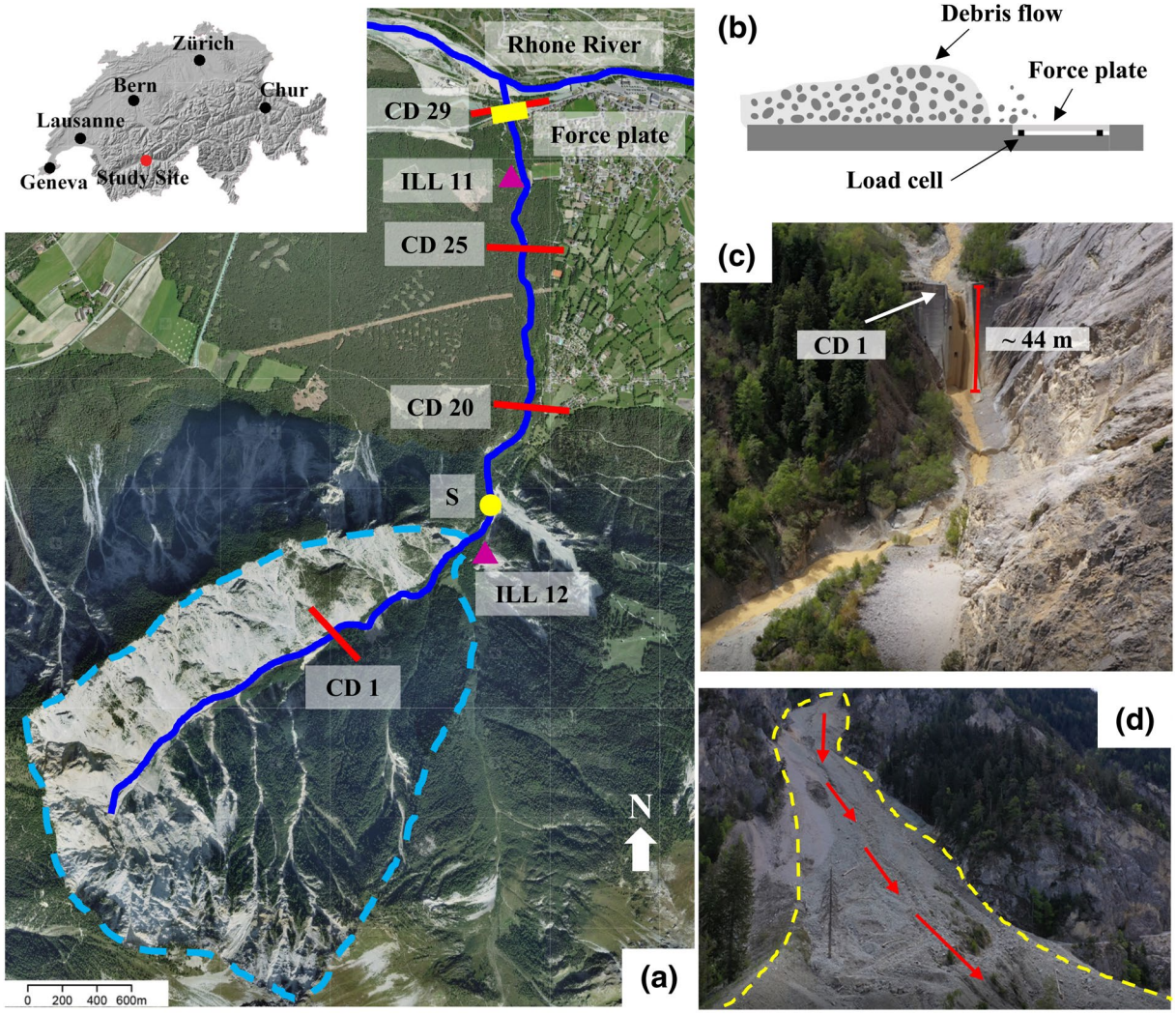

Figure 1. Study site. (a) Illgraben catchment (red dot in inset map marks location in Switzerland) with dashed blue line outlining the upper catchment. Solid blue lines represent the Illgraben torrent and Rhone River. Pink triangles are seismometer locations. Yellow rectangle indicates the force plate location. East side hillslope "Sagenschleif" connecting with the Illgraben canyon is marked at Point *S*. Red bars are the locations of selected check dams (CD). (b) Force plate sketch. (c) Photo of CD 1. (d) Photo of Sagenschleif. Dashed yellow line and arrows indicate outline and sliding direction of Sagenschleif.

In the last years, theoretical work has started to focus on seismic sources within the debris-flow mass (Allstadt et al., 2020; Farin et al., 2019; Kean et al., 2015; Lai et al., 2018) using the analogy to bedload transport in rivers (Tsai et al., 2012). The underlying idea is to express observed elastic ground motion as a response to ground impacts of debris-flow particles. However, the particle impact theory relies on parameters like particle velocities and particle size distributions, which are difficult to measure. Moreover, the relative contribution from horizontal and vertical impact forces both contributing to dominant seismic surface waves have been parameterized in an adhoc way (Farin et al., 2019). Consequently, variations in relative horizontal and vertical impact components, carrying information about channel bed and wall geometry or erosion cannot be resolved.

Here, we apply the particle impact theory using a series of well-documented debris flows at the Illgraben torrent (Switzerland, Figure 1). In order to separately estimate variations in relative horizontal and vertical impact components, we use a new approach to calculate seismic wave propagation. We observe that the force spectra inverted from seismic data near the torrent are coherent with in situ measurements at a force plate, and contain information about particle sizes, erosion, and deposition.

2. Study Site and Data

Located in southern Switzerland, the Illgraben catchment (area 8.9 km^2), extends from the summit of Mount Illhorn (2,716 m asl), through a fan, to the Rhone River (Hürlimann et al., 2003; Figure 1). Landslides and rockfalls occur regularly on steep slopes (~40°) in the upper catchment (Schlunegger et al., 2009) yielding sliding material, which stops downslope or directly in the Illgraben channel. These deposits transform into debris flows when the steep bedrock channels deliver large water discharge during heavy summer precipitation (Badoux et al., 2009; Bennett et al., 2013; Berger et al., 2011a). To minimize erosion of the channel, stabilize the channel bed, and enlarge discharge capacity, 29 Check Dams (CD) were installed along the channel (Figure 1c).

The debris-flow observatory by the Swiss Federal Institute for Forest, Snow, and Landscape Research (WSL) includes stage measurements, a force plate, in-torrent geophones, and video cameras similar to sensors of an early warning system (Badoux et al., 2009). The force plate, which was destroyed by a flow in 2016 and reinstalled in 2019 (design similar to that described by McArdell et al., 2007) is a 4 m wide (perpendicular to flow direction) and 2 m long (in flow direction) concrete slab within the channel bed just upstream of the brink of check dam 29 situated under a motorway bridge (Figures 1a and 1b). Measured vertical force is the sum of four load cells underneath the corners of the force plate. Herein, the vertical force data (collected at either 2,400 or 9,600 Hz) are grouped into adjacent nonoverlapping bins of 1 s duration, and the median value of the normal or horizontal forces are recorded for each bin. The concrete in the check dam upstream of the plate guides the flow onto the plate without abrupt changes in channel topography, thereby ensuring that the forces on the plate are generated by the weight of the flow (Figure S1). Boulder size is estimated at 1 s resolution from video recordings at CD 29 (Figure S2) by measuring the median axis (b axis) of all cobbles and boulders that were transported over CD 29. The resolution of the video recordings allows discrimination of particles with diameters larger than ~0.25 m. Below this size, Illgraben's debris flows contain a large amount of fine grains compared to other catchments (Hürlimann et al., 2019).

A laser sensor on the bridge above the force plate measures flow depth. The front velocity u_d of a flow is measured as the travel time from a check dam about 140 m upstream of the force plate (downstream of station ILL11) to the force plate. Calculations of event discharge, volume and bulk density are described by Schlunegger et al. (2009) and McArdell et al. (2007). Volume estimates are subject to uncertainties of up to 50% because their calculation accumulates uncertainties associated with flow rheology and partial sediment deposition on the force plate, especially after passage of the flow body. Flow depth, density, and velocity are accurate within 10% and weight measurement uncertainties are negligible compared to the other measurements. WSL staff are improving the accuracy of the bulk flow property estimates, so it is possible that the values reported herein may be updated when the final data set is published on the WSL data archive.

We use debris-flow seismograms recorded at a seismic network installed around the Illgraben catchment (Figure 1; Wenner et al., 2019). We selected the two stations closest to the channel (stations ILL11 and ILL12 in Figure 1, sampling rate: 100 Hz) that recorded 14 debris flows in 2018 and 2019, and for nine events in 2019 force plate measurements are available (Figure S1).

3. Methods

3.1. Particle Impact Sources

Elastic ground impact forces of grains of diameter D moving with velocity w_i can be expressed as (Tsai et al., 2012): $F_{0i} \approx 2mw_i$. For simplicity, and for large enough source-station distances, the boulder-rich debris-flow front dominates seismic signal generation (Farin et al., 2019). Stochastic impacts imply that the impact sum's spectrum over a time window length ΔT and over the area of the flow front is proportional to the spectrum of an individual impact (Tsai et al., 2012): $F_i(\omega, D) = F_{0i}(\omega, D)\sqrt{\frac{N(\omega, D)}{\Delta T}}$, where $\omega = 2\pi f$ is the angular frequency, f is frequency, i denotes the Cartesian force component (i = V for vertical and H for vector sum of two orthogonal horizontal directions), N is the total number of particle impacts with particle

size D over the area of the flow front. To simplify, we assume that the flow front area is the same for all events. The power spectral density (PSD) of the F_i^2 generated by stochastic particle impacts can then be expressed as:

$$F_i^2(\omega,D) = F_{0i}^2(\omega,D)\frac{N(\omega,D)}{\Delta T} \tag{1}$$

Integration of Equation 1 over all particle sizes over a given time window and over the area of the flow front yields the PSD of the apparent total impact forces: $F_{Ti}^2(\omega) = \int_D F_i^2(\omega,D)dD = \int_D F_{0i}^2(\omega,D)\frac{N}{\Delta T}dD$. We call $\left|F_{Ti}(\omega)\right|$ the Apparent Total Impact Force Spectra (AIFS). For simplicity, we assume that the AIFS is constant over a time window, which means that over the flow front it is the same over a channel section corresponding to a chosen time window.

Under the assumption of a particle impact velocity similar to the average flow front velocity u, AIFS have the following proportionality (Farin et al., 2019):

$$\text{AIFS} \propto \left[u^3 \int_D D^3 dD\right]^{\frac{1}{2}} \tag{2}$$

The integration over the grain size D distribution can be removed if one determines an effective particle diameter D_e, which may represent the 73rd percentile parameter D_{73} (Farin et al., 2019). Unfortunately, particle size distributions in torrents are rarely available (e.g., Rickenmann et al., 2012) and effective particle diameter is difficult to estimate.

3.2. Seismic Wave Propagation

As expected for particle ground impacts, seismic records at the surface are dominated by surface waves, which we assume propagate in a horizontally layered medium (e.g., Aki & Richards, 2002). The horizontal and vertical seismic signals contain the variations in relative horizontal and vertical impact components corresponding to the changes in channel bed topography. To facilitate analysis of the horizontal components of the seismic signals, we use a model of the vertical and horizontal PSD P_{OV} and P_{OH} of seismic signals from $F_{0V}(\omega,D)$ and $F_{0H}(\omega,D)$, which are the frequency spectra of vertical and horizontal impact forces for particle diameters D (Arai & Tokimatsu, 2004; Harkrider, 1964).

We simulate seismic wave propagation in terms of medium response functions L_{Rm} and L_{Lm} for Rayleigh and Love waves (Harkrider, 1964). The total PSD generated by the debris flows is then (see Supporting Information S1):

$$P_{TV}(\omega) \approx \sum_{m=0}^{M} L_{Rm}\left(2F_{TV}^2(\omega) + F_{TH}^2(\omega)\left(\frac{u}{w}\right)_m^2\right) \tag{3}$$

$$P_{TH}(\omega) \approx \sum_{m=0}^{M} L_{Rm}\left(\frac{u}{w}\right)_m^2\left(2F_{TV}^2(\omega) + F_{TH}^2(\omega)\left(\frac{u}{w}\right)_m^2\right) + L_{Lm}F_{TH}^2(\omega) \tag{4}$$

where the subscripts V and H denote vertical and horizontal directions, the subscripts R and L represent Rayleigh and Love waves. $L_{Rm} = A_{Rm}^2 e^{-2\xi k_{Rm} r} / \pi r k_{Rm}$, $L_{Lm} = A_{Lm}^2 e^{-2\xi k_{Lm} r} / \pi r k_{Lm}$, where A is the medium response factor (Harkrider, 1964), r is the source-to-station distance, u / w is the horizontal-to-vertical ratio of Rayleigh wave amplitudes on the free surface (Harkrider, 1964), ξ is the scattering damping ratio of soil (Arai & Tokimatsu, 2004), k is the wavenumber, and m is the mode value of Rayleigh and Love waves (for simplicity, we focus on the fundamental surface wave mode, $m = 0$).

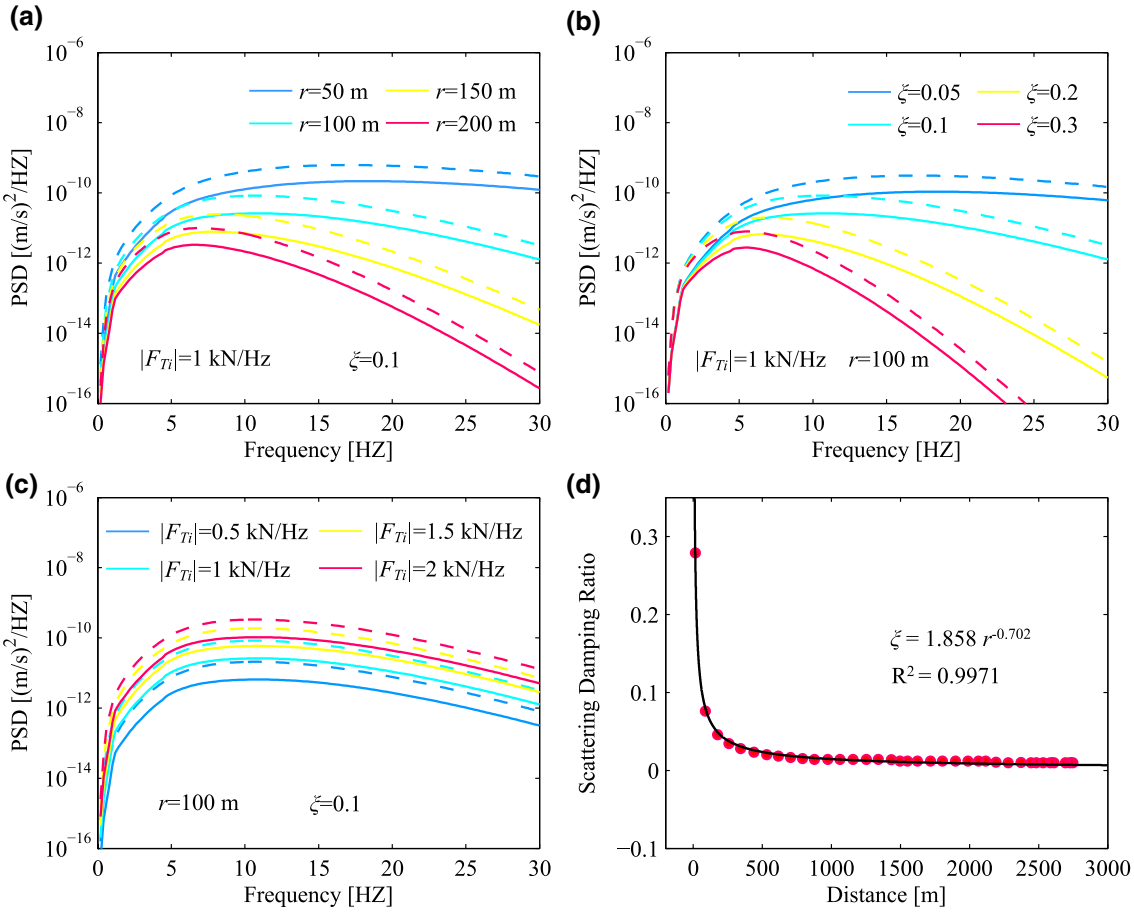

Figure 2. Sensitivity of PSDs to different parameters and evaluation of the scattering damping ratio of soil ξ. (a–c) Synthetic PSDs as a function of frequency for four different choices of r, ξ, and F_{Ti}. Solid and dashed lines correspond to vertical and horizontal PSDs. (d) The scattering damping ratio of soil ξ as a function of the source-to-station distance r. The solid line shows the damped least squares model fit.

In order to evaluate the AIFS ($|F_{TV}|$ and $|F_{TH}|$) from Equations 3 and 4, we need to estimate the seismic ground model, the average velocity of the debris-flow front u_u, the source-to-station distance r, and the scattering damping ratio of soil ξ (see Supporting Information S1).

We now evaluate the sensitivity of synthetic PSDs to parameters r and ξ (Figure 2). For increasing r or ξ, the amplitude and peak frequency of the PSD gradually decreases. However, the AIFS magnitude $|F_{Ti}|$ only affects the amplitude of the PSD, not the peak frequency. The distance dependence of the peak frequencies (Figure 2a) can be used to estimate locations of the debris-flow front (Lai et al., 2018; Wenner et al., 2019). Hence, when the peak frequency is measured for a known r, we can obtain the value of ξ to reproduce the measured peak frequency. Note that the values of ξ vary for different time windows reflecting changes of the subsurface and channel geometry along the runout path.

We inverted smoothed PSDs between 1 and 30 Hz using time windows between 10 and 40 s, depending on the average flow velocity (Supporting Information S2). Numerical tests show that including both horizontal and vertical components stabilizes the inversion compared to the vertical-only inversion (Supporting Information S3 and Figure S4).

4. Results

4.1. AIFS Scaling

We illustrate our approach with a debris flow on August 8, 2018 with likely the largest volume (ca. 100,000 m^3) since the installation of station ILL11. First, we estimate the average distance from the flow front to station ILL11 and the value of ξ for each time window using the method described above. Scour and fill of the debris material may locally change ξ. However, changes in ξ are likely only significant when erosion exposes bedrock (Kean et al., 2015), which is not the case on Illgraben's debris fan in the Rhone valley. Moreover, at Illgraben, changes in ξ concentrate near check dams (de Haas et al., 2020), such that spatial variations in ξ tend to cancel each other out leaving ξ unchanged between events. We observe an empirical relationship between ξ and distance r, which evolves over time depending on the flow front velocity (Figure 2d). We use this relationship to estimate ξ at a given time window for each event. Using the damped least squares inversion and the PSD of seismic signals in individual time windows, we invert for AIFS of the debris-flow front along the channel (Figures 3 and S5). To quantify the fit of the resulting AIFS, we calculate synthetic PSDs by inserting the AIFS back into the forward model (Equations 3 and 4). The synthetic PSDs are coherent with the measured PSDs (Figure S6). For other debris flows, the AIFS are estimated using the same approach.

We observe that at a source-to-receiver distance of about $r > 2{,}400$ m (corresponding to the along-flow distance from CD1 to the source of about $d < 1{,}000$ m) the PSD at station ILL11 is close to the noise level (Figure S6), even for large volume debris flows. As a representative value, we therefore use the average value of the vertical AIFS $\left|\bar{F}_{TV}\right|$ from $d \geq 1{,}000$ m. This averaging further cancels AIFS variations over short distance ranges of a few hundred meters, which result from changes in ξ attributed to scour and fill during previous events. Figure 3e shows a strong linear correlation between $\left|\bar{F}_{TV}\right|$ and the peak in vertical force generated by the debris-flow front F_{MV} measured at the force plate. The constant of proportionality α is 124.2. The correlation slightly rises from $R^2 = 0.8017$ to $R^2 = 0.8162$ for the scaling between $\bar{F}_{TV}^2$ against F_{MV} predicted by Farin et al. (2019) (Figures 3e and S7).

The F_{MV} scales linearly with bulk density ρ of the flow mixture and h_f: $F_{MV} = S_p \rho g h_f$, where S_p is the area of the force plate (8 m^2), and g is gravitational acceleration (9.8 m/s^2). Figure 3f shows the scaling between ρh_f and $\left|\bar{F}_{TV}\right|$ with a proportionality constant $\beta = 1.616$. The similarity between α (124.2) and $S_p g \beta$ (126.7) bolsters the linear correlation between $\left|\bar{F}_{TV}\right|$ and the measured data (F_{MV} and ρh_f).

As a first approximation, we ignore the contribution of water to the flow weight, so the weight measurement F_{MV} at the force plate is proportional to D^3 integrated over all grain sizes. This circumvents the need to determine specific grain size distributions. The video analysis (Figure S2) only considers the largest particles and thus does not provide grain size distribution or effective particle sizes. Figure 3g shows the scaling between $\left|\bar{F}_{TV}\right|$ and $D_{\max}^{1.5}$, which should be linear if $D_{\max}^{1.5}$ scaled linearly with D_{73} and the flow velocity between events were the same (Equation 2, Farin et al., 2019). Although a linear trend is reasonable, the correlation is smaller than the one between $\left|\bar{F}_{TV}\right|$ and F_{MV} ($R^2 = 0.6831$ compared to $R^2 = 0.8017$; Figure 3e), which may at least partially result from different particle size distributions.

4.2. AIFS Variations

Though subject to uncertainties, we expect that our volume estimates separate small and large events. For debris flows with small volumes (estimated $V \leq 35{,}000$ m^3, except the July 15, 2019 event, see Table S2), the horizontal and vertical AIFS's show a decreasing trend along the flow path (Figures 3b, 3d, and S5). Note that for June 20, 2019 event, the seismic stations recorded ground vibrations (Figure S8), but the force plate did not record a debris-flow event, which means that this event stopped along the flow path before reaching CD 29. In contrast, for large volume flows ($V > 35{,}000$ m^3), the AIFS gradually increase during run out until reaching CD25. Exceptions to this trend are discussed in Supporting Information S5.

Small volume events show less AIFS variations along the flow path (Figure 3b and S5b). When interpreting the AIFSs (Figure 3b), we therefore focus on debris flows with large volumes starting at $d = 1{,}000$ m. For

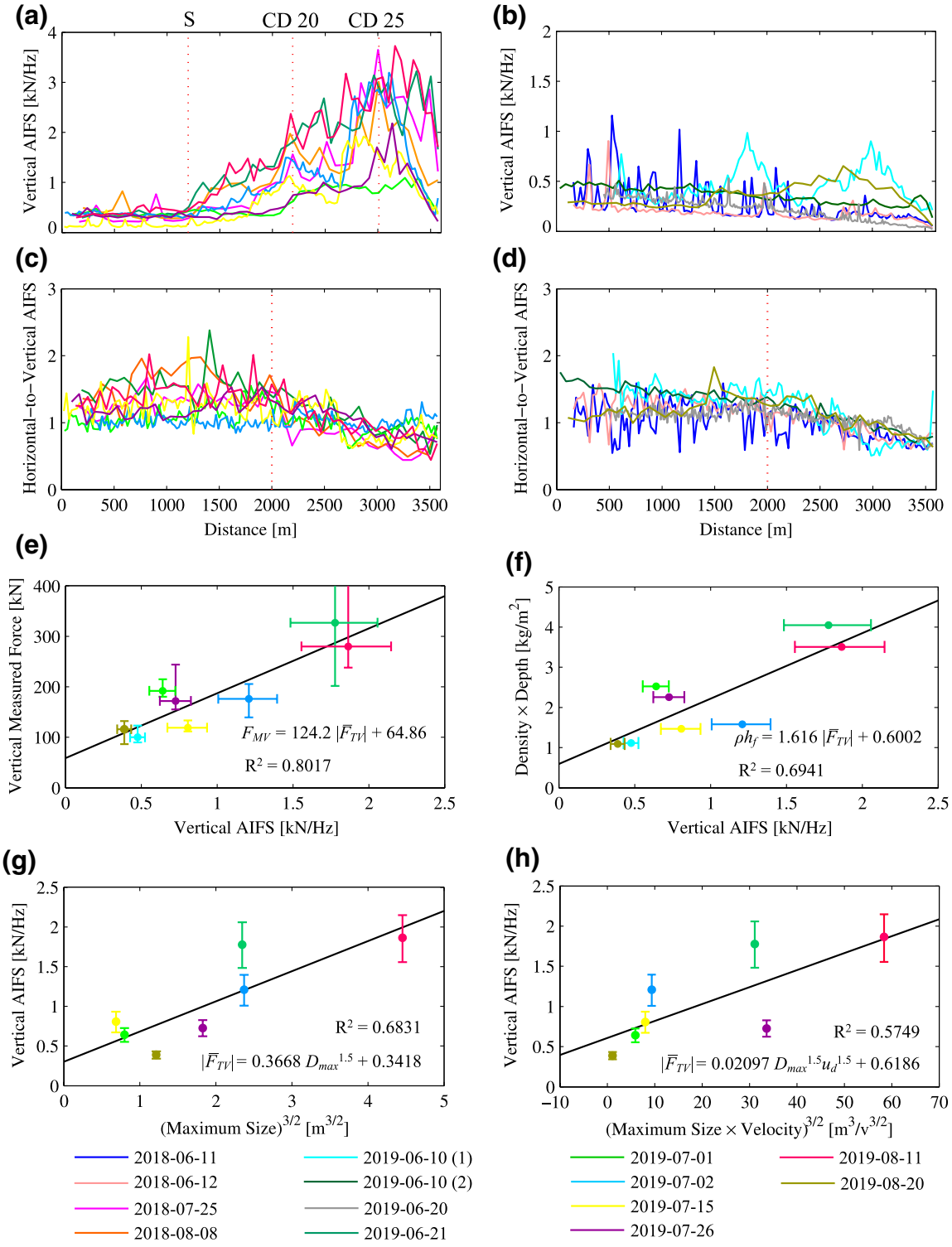

Figure 3. Apparent total impact force spectra (AIFS). Panels (a and b) are the vertical AIFS along the flow path for events with large (estimated $V > 35{,}000$ m^3) and small (estimated $V \leq 35{,}000$ m^3 except the July 15, 2019 event) volumes. Distance is measured from Check Dam 1 (CD1), past the confluence with the Sagenschleif tributary (Point *S*, indicated in Figure 1). (c and d) The ratios between horizontal and vertical AIFS for large and small events. (e) The average values of vertical AIFS $\left|\bar{F}_{TV}\right|$ versus the F_{MV}. The solid line is the least squares regression. Panel (f) shows ρh_f versus $\left|\bar{F}_{TV}\right|$ (h_f is flow depth corresponding to F_{MV} and ρ is bulk density). Panel (g) shows $\left|\bar{F}_{TV}\right|$ versus $D_{\max}^{1.5}$. Panel (h) shows $\left|\bar{F}_{TV}\right|$ versus $D_{\max}^{1.5} u_d^{1.5}$. Uncertainties in panels (e–h) are calculated as described in Supporting Information S4.

large events, the vertical and horizontal AIFS start to increase gradually at a distance of $d = 1{,}150$ m (Point *S* in Figure 1). This also marks the confluence of the Illgraben channel and a steep lateral slope to the east of it, called Sagenschleif (Figure 1d). In recent years, Sagenschleif has produced mass wasting events, including minor debris flows, providing sediments to the Illgraben channel (de Haas et al., 2020). Entrainment of these sediments can increase the debris-flow volume and impact forces during runout events in the main canyon.

At about $d = 2{,}100$ m, an AIFS peak corresponds to the debris flows passing CD 20 (Figure 3). With a height of about 10 m, this is the largest check dam for $d > 1{,}000$ m. As debris undergoes free fall from the top of the check dam it generates strong vertical ground impacts. Erosion is most pronounced at the downstream side of a check dam (Berger et al., 2011a) and entrained particle impacts are expected to increase AIFS downstream of a check dam. Subsequently, another peak in vertical AIFS corresponds to the position of CD 25. With a height of about 7 m, this check dam is the second largest check dam for $d > 1{,}000$ m. Other peaks in vertical AIFS may also relate to check dams. This is, however, difficult to assess, because other check dams are smaller (about 0.8–5.3 m), and debris flows undergo longitudinal elongation resulting in material crossing multiple check dams at a given time.

The spatial patterns of horizontal AIFS are similar to the vertical ones (Figures 3 and S5). For most events, horizontal-to-vertical AIFS ratios decrease after $d = 2{,}000$ m (Figures 3c and 3d). Ground properties (e.g., Farin et al., 2018) and particle collision modes (e.g., Cole et al., 2009) may explain this change in signal polarization.

5. Discussion and Conclusions

We highlight two key findings of our study (Figure 3):

Finding 1: Apparent total impact force spectra (AIFSs) averaged over the lower part of Illgraben scale with force plate measurements.

Finding 2: During runout, AIFS increase for large events and decrease for small events.

To derive the scaling $\left|\bar{F}_{TV}\right| \sim D^{1.5}u_d^{1.5}$, Farin et al., (2019) assume that impact velocities are given by stochastic particle velocity fluctuations resulting from particle-bed rather than particle-particle collisions. For free falling particles downstream of check dams, this assumption is unlikely satisfied, which explains why the correlation between F_{MV} ($\sim D^3$) and $\left|\bar{F}_{TV}\right|$ found in this study (*Finding 1*) does not include a reference to flow velocity u_d. In fact, including the factor of ${u_d}^{1.5}$, the correlation between $\left|\bar{F}_{TV}\right|$ and the impact force model drops from $R^2 = 0.6831$ to $R^2 = 0.5749$ (Figures 3g and 3h). A lack of a single representative value of u_d is also supported by a low correlation between u_u and u_d (Figure S9), which indicates that the flow front velocity changes along the path. Another complication is that previous observations at Illgraben showed that velocities of particles with a given size depend on water content and thus vary between events (McArdell et al., 2003). This suggests that a scalar parameter describing particle impact velocities as used in Farin et al. (2019) may not be transferable between events. Finally, the impact rates are derived under the assumption that particles interact elastically with bed roughness, whose length scale equals the particle diameter. This influences the dependence of $\left|\bar{F}_{TV}\right|$ on D, and may be an oversimplification. First, elasticity may not be fully satisfied for soft sediment covers in Illgraben's bed. Second, a dominant roughness length scale seems unlikely for free falling particles. This may be the reason why our observed scaling between $\left|\bar{F}_{TV}\right|$ and particle size D, departs from the resulting theoretical prediction ($D^{1.5}$ rather than D^3). Nevertheless, our scaling of AIFS with boulder sizes and flow front mass is in line with previously found correlations between kinetic energy of debris flow surges and seismic energy (Coviello et al., 2019; Figure S10).

Our AIFS averaging might also seem an oversimplification, because AIFS is a nonstationary process (Figure 3). Notwithstanding, such averaging is a natural choice for less well-documented events in other environments. Although the exact scaling is difficult to verify even for a nearly ideal natural laboratory such as the Illgraben, our results show that the theoretical basis by Farin et al. (2019) identifies particularly destructive events with large boulder sizes (Figure 3g). This is not necessarily expected, because the force

plate measurement is proportional to volume (or weight) of all particles integrated over all sizes rather than the maximum boulder size. However, since both integrated particle volumes (Figure 3e) and maximum boulder size (Figure 3g) correlate reasonably with impact forces, the effect of grain size distributions varying between events seems secondary (see Supporting Information S6 for further discussion on model assumptions).

Finding 2 is likely related to erosion, deposition, flow velocity change, and size-segregation along the channel. Erosion at the lee side of check dams can contribute to the increase in AIFS during runout. Significant erosion and entrainment for Illgraben's larger events is expected, because for such events landslide deposits constituting debris-flow sources in the upper catchment are one order of magnitude smaller than the resulting debris flows (Berger et al., 2011b). In contrast, events with low flow depths are more likely to deposit material on the lower Illgraben part (Schürch et al., 2011). In our data set, such shallow events are small volume events (Table S2) explaining decreasing AIFS along the debris-flow runout (Figures 3b and 3d). For the small June 10, 2019 events, drone-derived imagery did confirm unusually strong deposition between 1,200 and 700 m upstream of CD29, locally increasing bed elevation by more than 2 m (de Haas et al., 2020). Furthermore, accounts of debris flows that stop before CD29 (such as the June 20, 2019 event) suggest that small events decelerate as they approach the force plate. Although our measurements do not resolve velocity variations of debris flows, this deceleration may contribute to decreasing AIFS.

The discussion about erosion and deposition effects on AIFS should not be oversimplified: Erosion is expected to increase AIFS when entrained particle diameters significantly increase some effective diameter, such as D_{73}. Similarly, deposition dampens AIFS if deposited particles efficiently lower this effective size. The latter is more likely to be the case for shallow events, which lack large boulders. Entrainment of boulders with sizes near D_{73} and larger in the lower Illgraben part is less likely, because availability of such large boulders is rarely observed here. In addition, although erosion has a potential influence on the elastic properties of the bed, this influence is more significant in the upstream part of the flow path. This demands another mechanism, which explains AIFS increases of large events. We propose the mechanism, which concentrates boulders at the flow front as documented by Pierson (1986) and Johnson et al. (2012). As a result of particle sorting, coarse material segregates to the flow surface and is transported to the flow front. Coarse material in the flow front is overridden, then recirculates in spiral trajectories due to size-segregation. This "conveyor-belt behavior" concentrates boulders at the front and increases its thickness or at least counteracts particle deposition. Since our AIFS calculations trace the flow front, the increasing boulder concentration during runout explains the AIFS increase (Figures 3a and S5a). This mechanism is less pronounced for small events, which tend to resemble debris floods with lower densities and thus a weaker conveyor-belt behavior.

We conclude that although we ignored flow velocity, grain size distributions, and fluid/particle fraction differing between events, our study shows that simple estimates of emitted seismic energy scale with a power of boulder sizes. In this way, seismic measurements may serve as an efficient way to process seismic data in order to automatically identify and warn against particularly destructive events.

Acknowledgments
We thank Victor Tsai, Velio Coviello, and two anonymous reviewers for their thoughtful reviews of the manuscript. Seismometer deployments were funded by WSL and the Canton Valais and supported by the Swiss Military. We thank the Swiss Seismological Service and its Electronic Laboratory (ELAB) for technical support. This work was supported by the National Key Research and Development program of China (Project No. 2017YFC1501003), the Major Program of the National Natural Science Foundation of China (Grant No. 41790433), and the National Natural Science Foundation of China (Grant No. 41772312).

Data Availability Statement

All seismic data are openly available via the Swiss Seismological Service, http://arclink.ethz.ch/webinterface. Force plate measurements, flow depth data and boulder data are available at https://doi.org/10.3929/ethz-b-000437719.

References

Aki, K., & Richards, P. G. (2002). *Quantitative seismology*, 2nd ed., Sausalito, CA: University Science Books.

Allstadt, K. (2013). Extracting source characteristics and dynamics of the August 2010 Mount Meager landslide from broadband seismograms. *Journal of Geophysical Research Earth Surface*, *118*(3), 1472–1490. https://doi.org/10.1002/jgrf.20110

Allstadt, K., Farin, M., Iverson, R. M., Obryk, M. K., Kean, J. W., Tsai, V. C., et al. (2020). Measuring basal force fluctuations of debris flows using seismic recordings and empirical green's functions. *Journal of Geophysical Research: Earth Surface*, *125*, e2020JF005590. https://doi.org/10.1029/2020JF005590

Arai, H., & Tokimatsu, K. (2004). S-wave velocity profiling by inversion of microtremor H/V spectrum. *Bulletin of the Seismological Society of America*, *94*(1), 53–63. https://doi.org/10.1785/0120030028

Badoux, A., Graf, C., Rhyner, J., Kuntner, R., & McArdell, B. W. (2009). A debris-flow alarm system for the alpine Illgraben catchment: Design and performance. *Natural Hazards*, *49*(3), 517–539. https://doi.org/10.1007/s11069-008-9303-x

Barrière, J., Oth, A., Hostache, R., & Krein, A. (2015). Bed load transport monitoring using seismic observations in a low-gradient rural gravel bed stream. *Geophysical Research Letters*, *42*, 2294–2301. https://doi.org/10.1002/2015GL063630

Bennett, G. L., Molnar, P., McArdell, B. W., Schlunegger, F., & Burlando, P. (2013). Patterns and controls of sediment production, transfer and yield in the Illgraben. *Geomorphology*, *188*, 68–82. https://doi.org/10.1016/j.geomorph.2012.11.029

Berger, C., McArdell, B. W., & Schlunegger, F. (2011a). Direct measurement of channel erosion by debris flows, Illgraben, Switzerland. *Journal of Geophysical Research*, *116*, F01002. https://doi.org/10.1029/2010JF001722

Berger, C., McArdell, B. W., & Schlunegger, F. (2011b). Sediment transfer patterns at the Illgraben catchment, Switzerland: Implications for the time scales of debris flow activities. *Geomorphology*, *125*(3), 421–432. https://doi.org/10.1016/j.geomorph.2010.10.019

Burtin, A., Vergne, J., Rivera, L., & Dubernet, P. (2010). Location of river-induced seismic signal from noise correlation functions. *Geophysical Journal International*, *182*(3), 1161–1173. https://doi.org/10.1111/j.1365-246X.2010.04701.x

Cole, S. E., Cronin, S. J., Sherburn, S. & Manville, V. (2009). Seismic signals of snow-slurry lahars in motion: 25 September 2007, Mt Ruapehu, New Zealand. *Geophysical Research Letters*, *36*(9), 1–5. https://doi.org/10.1029/2009GL038030

Coviello, V., Arattano, M., Comiti, F., Macconi, P., & Marchi, L. (2019). Seismic characterization of debris flows: Insights into energy radiation and implications for warning, *Journal of Geophysical Research: Earth Surface*, *124*(6), 1440–1463. https://doi.org/10.1029/2018jf004683

Dammeier, F., Moore, J. R., Hammer, C., Haslinger, F., & Loew, S. (2016). Automatic detection of alpine rockslides in continuous seismic data using hidden Markov models. *Journal of Geophysical Research: Earth Surface*, *121*(2), 351–371. https://doi.org/10.1002/2015JF003647

de Haas, T., Nijland, W., de Jong, S. M., & McAdrell, B. W. (2020). How memory effects, check dams, and channel geometry control erosion and deposition by debris flows. *Scientific Reports*, *10*, 14024. https://doi.org/10.1038/s41598-020-71016-8

Ekström, G., & Stark, C. P. (2013). Simple scaling of catastrophic landslide dynamics. *Science*, *339*(6126), 1416–1419. https://doi.org/10.1126/science.1232887

Farin, M., Mangeney, A., de Rosny, J., Toussaint, R., & Trinh, P. T. (2018). Link between the dynamics of granular flows and the generated seismic signal: Insights from laboratory experiments. *Journal of Geophysical Research: Earth Surface*, *123*, 1407–1429. https://doi.org/10.1029/2017JF004296

Farin, M., Tsai, V. C., Lamb, M. P., & Allstadt, K. E. (2019). A physical model of the high-frequency seismic signal generated by debris flows. *Earth Surface Processes and Landforms*, *44*(13), 2529–2543. https://doi.org/10.1002/esp.4677

Gimbert, F., Tsai, V. C., & Lamb, M. P. (2014). A physical model for seismic noise generation by turbulent flow in rivers. *Journal of Geophysical Research: Earth Surface*, *119*, 2209–2238. https://doi.org/10.1002/2014JF003201

Harkrider, D. G. (1964). Surface waves in multilayered elastic media I. Rayleigh and Love waves from buried sources in a multilayered elastic half-space. *Bulletin of the Seismological Society of America*, *54*(2), 627–679.

Hibert, C., Ekström, G., & Stark, C. P. (2017). The relationship between bulk-mass momentum and short-period seismic radiation in catastrophic landslides: Landslides short-period seismic signals. *Journal of Geophysical Research: Earth Surface*, *122*(5), 1201–1215. https://doi.org/10.1002/2016JF004027

Hibert, C., Mangeney, A., Grandjean, G., & Shapiro, N. M. (2011). Slope instabilities in Dolomieu crater, Réunion Island: From seismic signals to rock fall characteristics. *Journal of Geophysical Research: Earth Surface*, *116*, F04032. https://doi.org/10.1029/2011JF002038

Hürlimann, M., Coviello, V., Bel, C., Guo, X., Berti, M., Graf, C., et al. (2019). Debris-flow monitoring and warning: Review and examples. *Earth-Science Review*, *199*, 102981. https://doi.org/10.1016/j.earscirev.2019.102981

Hürlimann, M., Rickenmann, D., & Graf, C. (2003). Field and monitoring data of debris-flow events in the Swiss Alps. *Canadian Geotechnical Journal*, *40*(1), 161–175. https://doi.org/10.1139/t02-087

Iverson, R. M. (1997). The physics of debris flows. *Reviews of Geophysics*, *35*, 245–296. https://doi.org/10.1029/97RG00426

Iverson, R. M. (2003). The debris-flow rheology myth. *Paper presented at Debris-Flow Hazards Mitigation: Mechanics, Prediction, and Assessment, Chengdu, China* (Vol. *1*, 303–314). Rotterdam, Netherlands:Millpress.

Iverson, R. M., & Vallance, J. W. (2001). New views of granular mass flow. *Geology*, *29*, 115–118. https://doi.org/10.1130/0091-7613(2001)029<0115:NVOGMF>2.0.CO;2

Johnson, C. G., Kokelaar, B. P., Iverson, R. M., Logan, M., LaHusen, R. G., & Gray, J. M. N. T. (2012). Grain-size segregation and levee formation in geophysical mass flows. *Journal of Geophysical Research*, *117*, F01032. https://doi.org/10.1029/2011JF002185

Kean, J., Coe, J., Coviello, V., Smith, J., McCoy, S., & Arattano, M. 2015. Estimating rates of debris flow entrainment from ground vibrations. *Geophysical Research Letters*, *42*, 6365–6372. https://doi.org/10.1002/2015GL064811

Lai, V. H., Tsai, V. C., Lamb, M. P., Ulizio, T. P., & Beer, A. R. (2018). The seismic signature of debris flows: Flow mechanics and early warning at Montecito, California. *Geophysical Research Letters*, *45*, 5528–5535. https://doi.org/10.1029/2018GL077683

Marchetti, E., Walter, F., Barfucci, G., Genco, R., Wenner, M., Ripepe, M., et al. (2019). Infrasound array analysis of debris flow activity and implication for early warning. *Journal of Geophysical Research: Earth Surface*, *124*, 567–587. https://doi.org/10.1029/2018JF004785

McArdell, B. W., Bartelt, P., & Kowalski, J. (2007). Field observations of basal forces and fluid pore pressure in a debris flow. *Geophysical Research Letters*, *34*, L07406. https://doi.org/10.1029/2006GL029183

McArdell, B., Guglielmetti, S., & Swartz, M. (2003). *Observations of coarse particle motion in debris flows and the application to numerical modeling*. Paper presented at EGS-AGU-EUG Joint Assembly, Nice, France.

Moretti, L., Mangeney, A., Stutzmann, E., Huggel, C., Schneider, D., & Bouchut, F. (2012). Numerical modeling of the Mount Steller landslide flow history and of the generated long period seismic waves. *Geophysical Research Letters*, *39*(16), 276–289. https://doi.org/10.1029/2012GL052511

Ogiso, M., & Yomogida, K. (2015). Estimation of locations and migration of debris flows on Izu-Oshima Island, Japan, on 16 October 2013 by the distribution of high frequency seismic amplitudes. *Journal of Volcanology and Geothermal Research*, *298*, 15–26. https://doi.org/10.1016/j.jvolgeores.2015.03.015

Pierson, T. C. (1986). Flow behavior of channelized debris flows, Mount St. Helens, Washington. In A. D. Abrahams(Ed.), *Hillslope processes*(pp. 269–296). Boston, MA: Allen and Unwin.

Rickenmann, D., Turowski, J. M., Fritschi, B., Klaiber, A., & Ludwig, A. (2012). Bedload transport measurements at the Erlenbach stream with geophones and automated basket samplers. *Earth Surface Processes and Landforms*, *37*(9), 1000–1011.

Schimmel, A., & Hübl, J. (2015). Approach for an early warning system for debris flows based on acoustic signals. In G. Lollino, et al. (Ed.), Engineering geology for society and territory (Vol. 3, pp. 55–58). Cham, Switzerland: Springer.

Schimmel, A., & Hübl, J. (2016). Automatic detection of debris flows and debris floods based on a combination of infrasound and seismic signals. *Landslides*, *13*(5), 1181–1196. https://doi.org/10.1007/s10346-015-0640-z

Schimmel, A., Hübl, J., McArdell, B. W., & Walter, F. (2018). Automatic identification of alpine mass movements by a combination of seismic and infrasound sensors. *Sensors*, *18*(5), 1658. https://doi.org/10.3390/s18051658

Schlunegger, F., Badoux, A., McArdell, B. W., Gwerder, C., Schnydrig, D., Rieke-Zapp, D., & Molnar, P. (2009). Limits of sediment transfer in an alpine debris-flow catchment, Illgraben, Switzerland. *Quaternary Science Reviews*, *28*, 1097–1105.

Schürch, P., Densmore, A. L., Rosser, N. J., & McArdell, B. W. (2011). Dynamic controls on erosion and deposition on debris-flow fans. *Geology*, *39*(9), 827–830.

Tsai, V. C., Minchew, B., Lamb, M. P., & Ampuero, J.-P. (2012). A physical model for seismic noise generation from sediment transport in rivers. *Geophysical Research Letters*, *39*, L02404. https://doi.org/10.1029/2011GL050255

Walter, F., Burtin, A., McArdell, B. W., Hovius, N., Weder, B., & Turowski, J. M. (2017). Testing seismic amplitude source location for fast debris-flow detection at Illgraben, Switzerland. *Natural Hazards and Earth System Sciences*, *17*(6), 939–955. https://doi.org/10.5194/nhess-17-939-2017

Wenner, M., Walter, F., McArdell, B., & Farinotti, D. (2019). Deciphering debris-flow seismograms at Illgraben, Switzerland. In J. W. Kean, J. A. Coe, P. M. Santi, & B. K. Guillen (Eds.), In *Association of environmental and engineering geologists; special publication 28*.St. Golden, CO: Colorado School of Mines. Arthur Lakes Library.

References From the Supporting Information

Aster, R. C., Borchers, B., & Thurber, C. H. (2005). *Parameter estimation and inverse problems*. Amsterdam, the Netherlands: Elsevier.

Picozzi, M., & Albarello, D. (2007). Combining genetic and linearized algorithms for a two-step joint inversion of Rayleigh wave dispersion and H/V spectral ratio curves. *Geophysical Journal International*, *169*(1), 189–200. https://doi.org/10.1111/j.1365-246X.2006.03282.x